A numerical 1.5D method for the rapid simulation of geophysical resistivity measurements

M. Shahriari [1], S. Rojas [5], D. Pardo [2,1,3], A. Rodríguez-Rozas [1,2], S. A. Bakr [4,1], V. M. Calo [5,6,7], I. Muga [8]

[1] Basque Center for Applied Mathematics, (BCAM), Bilbao, Spain.
[2]University of the Basque Country (UPV/EHU), Leioa, Spain.
[3]Ikerbasque (Basque Foundation for Sciences), Bilbao, Spain.
[4]Department of Mathematics, Assiut University, Assiut, Egypt.
[5]Applied Geology, Western Australian School of Mines, Faculty of Science and Engineering, Curtin University, Perth, WA, Australia.
[6]Mineral Resources, Commonwealth Scientific and Industrial Research Organisation (CSIRO), Kensington, WA, Australia.
[7]Curtin Institute for Computation, Curtin University, Perth, WA, Australia.
[8]Instituto de Matemáticas, Pontificia Universidad Católica de Chile, Valparaíso, Chile.
*correspondence to: Mostafa Shahriari, BCAM-Basque Center for Applied Mathematics, Mazarredo 14, E48009 Bilbao, Spain; E-mail: m.shahriari.sh@gmail.com[1]

Abstract

In some geological formations, borehole resistivity measurements can be simulated using a sequence of 1D models. By considering a 1D layered media, we can reduce the dimensionality of the problem from 3D to 1.5D via a Hankel transform. The resulting formulation is often solved via a semi-analytic method, mainly due to its high performance. However, semi-analytic methods have important limitations such as, for example, their inability to model piecewise linear variations on the resistivity. Herein, we develop a multi-scale finite element method (FEM) to solve the secondary field formulation. This numerical scheme overcomes the limitations of semi-analytic methods while still delivering high performance.

Keywords: logging-while-drilling (LWD), resistivity measurements, finite element method, Hankel transform, multi-scale method, secondary field

1. Introduction

Logging-while-drilling (LWD) is a technique that conveys borehole logging tools (e.g., gamma ray, resistivity, density, and sonic) downhole and record measurements while the hole is being drilled [1]. These tools provide two pieces of information: (a) real-time data, which is processed on the field while drilling, and (b) information that is stored in the device to process after pulling it out from the hole. We use real-time data to evaluate the formation for geosteering, which is the act of adjusting inclination and azimuth angles of the borehole to reach a geological target [1–5].

The first commercial LWD tool appeared in the 1970's. They were commercially used for formation evaluation, especially in high-angle wells. Nowadays, LWD tools are mostly used for geosteering applications. Modern borehole resistivity instruments can measure all nine components of the magnetic field, namely xx, xy, xz, yx, yy, yz, zx, zy and zz couplings (the first letter indicates the orientation of the transmitter and the second one indicates the receiver orientation) [6–8].

Since the depth of investigation of LWD resistivity measurements is limited compared to the assumed thickness of the geological layers, it is common to approximate subsurface models in the proximity of the logging instrument with a sequence of 1D models [1, 9–11]. In a 1D model, we reduce the dimension of the problem via a Hankel or a 2D Fourier transform along the directions over which we assume the material properties to be invariant [12–18]. The resulting ordinary differential equations (ODEs) can be solved (a) analytically, leading to a semi-analytic approach after the numerical inversion of a Hankel transform [12, 19–23], or (b) numerically, leading to a numerical approach [24].

Solving the ODEs analytically has some major limitations, for example, (a) it is only possible to consider piecewise constant material properties, and in particular, piecewise-linear resistivity distributions cannot be solved analytically; (b) a specific set of cumbersome formulas has to be derived for each physical process (e.g., electromagnetism, elasticity, etc.) anisotropy type, etc.; (c) analytical

derivatives of certain models (e.g., cross-bedded formations, or derivatives with respect to the bed boundary positions) are often difficult to obtain and have not been published to the best of our knowledge [6].

Solving the resulting ODEs numerically is also possible. In [24], the authors use a 2D Fourier transform to reduce the dimension of the problem. Then, they employ a highly accurate 1D finite difference method (FDM) to solve the ODEs. This method is relatively simple to implement. However, this combined methodology has the following limitations, which reduce the speed of the method: (a) for each tool position, they solve a new system of equations, which is relatively large; and (b) by using a 2D Fourier transform, the resulting number of 1D problems (associated with each Fourier mode) is larger than those arising from employing a Hankel transform. The use of other traditional techniques such as a finite element method (FEM) (see, e.g., [25]) to solve the resulting ODEs would not alleviate those problems.

Our main contribution is to overcome the above limitations of both semi-analytic and existing numerical methods by solving each 1D problem (associated with a Hankel mode) using an efficient multi-scale FEM. Our multi-scale method has the following advantages: (a) we can consider arbitrary resistivity distributions along the 1D direction, and (b) we can easily and rapidly construct derivatives with respect to the material properties and position of the bed boundaries by using an adjoint formulation, which allows us to compute numerically the derivatives forming the Jacobian matrix needed by the Gauss-Newton inversion method at (almost) no additional cost. Despite these advances, presently our proposed multi-scale method is slower than the semi-analytic one.

The paper is organized as follows: Section 2 describes the strong and weak (variational) formulations. Section 3 derives the 1.5D variational formulation using a Hankel transform, and a rotation matrix to simplify the computations. Section 4 details the proposed multi-scale FEM. Section 5 provides the relevant implementation details. In Section 6, we illustrate the accuracy and performance of our method via numerical experimentation. Section 7 delineates the summary, conclusions, and future work.

2. 3D Formulation

In this section, we describe the strong and weak formulations for our three dimensional (3D) electromagnetic (EM) problem.

2.1. Strong formulation

Let $\boldsymbol{\sigma}(x, y, z)$ be the real-valued conductivity tensor with positive determinant. Let $\mathbf{J}$ be a volumetric current source density and $\mathbf{M}$ a magnetic source flux density. Then, the EM fields satisfy Maxwell's equations in 3D space:

$$\nabla \times \boldsymbol{\mathcal{H}} = (\boldsymbol{\sigma} - i\omega\boldsymbol{\varepsilon})\,\boldsymbol{\mathcal{E}} + \mathbf{J}, \tag{1}$$

$$\nabla \times \boldsymbol{\mathcal{E}} = i\omega\boldsymbol{\mu}\boldsymbol{\mathcal{H}} + i\omega\boldsymbol{\mu}\mathbf{M}, \tag{2}$$

where $\boldsymbol{\mathcal{E}}$ is the complex-valued electric field, $\boldsymbol{\mathcal{H}}$ is the magnetic field, $\omega = 2\pi f$ is the angular frequency, where $f > 0$ is the frequency of the transmitter, $\boldsymbol{\varepsilon}$ and $\boldsymbol{\mu}$ are the permittivity and magnetic permeability tensors of the media, respectively, and i is the imaginary unit, $i^2 = -1$. The problem domain is $\Omega = \mathbb{R}^3$. By pre-multiplying (1) by $\tilde{\boldsymbol{\sigma}}^{-1} = (\boldsymbol{\sigma} - i\omega\boldsymbol{\varepsilon})^{-1}$, applying the curl operator, and substituting (2) into the result, we arrive at the following reduced wave equation for the magnetic field:

$$\nabla \times \tilde{\boldsymbol{\sigma}}^{-1}\nabla \times \boldsymbol{\mathcal{H}} - i\omega\boldsymbol{\mu}\boldsymbol{\mathcal{H}} = \mathbf{R}, \tag{3}$$

where the right-hand-side is:

$$\mathbf{R} = i\omega\boldsymbol{\mu}\mathbf{M} + \nabla \times \tilde{\boldsymbol{\sigma}}^{-1}\mathbf{J}.$$

In order to ensure the uniqueness of the magnetic field, we use the Silver-Müller radiation condition [3, 5, 25].

2.2. Weak formulation

Let $\boldsymbol{\mathcal{F}}$ be an arbitrary test function and $\boldsymbol{\mathcal{F}}^*$ its conjugate transpose. Pre-multiplying Equation (3) by $\boldsymbol{\mathcal{F}}^*$ and integrating over the domain Ω, we obtain the following equation:

$$\int_\Omega \boldsymbol{\mathcal{F}}^*(\nabla \times \tilde{\boldsymbol{\sigma}}^{-1}\nabla \times \boldsymbol{\mathcal{H}})d\Omega - i\omega \int_\Omega \boldsymbol{\mathcal{F}}^*\boldsymbol{\mu}\boldsymbol{\mathcal{H}}d\Omega = \int_\Omega \boldsymbol{\mathcal{F}}^*\mathbf{R}d\Omega. \tag{4}$$

In the above, as a sufficient condition to ensure integrability, we select $\boldsymbol{\mathcal{F}} \in H(\mathbf{curl}; \Omega)$, where:

$$H(\mathbf{curl}; \Omega) = \{\boldsymbol{\mathcal{F}} \in (L^2(\Omega))^3 : \nabla \times \boldsymbol{\mathcal{F}} \in (L^2(\Omega))^3\}.$$

Using integration by parts assuming that the solution and its flux are continuous, and considering the radiation condition, we obtain the following variational formulation:

$$\int_\Omega (\nabla \times \boldsymbol{\mathcal{F}})^* (\tilde{\boldsymbol{\sigma}}^{-1} \nabla \times \boldsymbol{\mathcal{H}}) d\Omega - i\omega \int_\Omega \boldsymbol{\mathcal{F}}^* \boldsymbol{\mu} \boldsymbol{\mathcal{H}} d\Omega = \int_\Omega \boldsymbol{\mathcal{F}}^* \mathbf{R} d\Omega. \tag{5}$$

3. 1.5D Formulation

In our model problem, we consider the 3D Maxwell's equations in a 1D transversely isotropic (TI) layered formation. That is, the formation conductivity is constant along the x and y directions, and the conductivity tensor is defined as:

$$\boldsymbol{\sigma}(z) = \begin{pmatrix} \sigma_h(z) & 0 & 0 \\ 0 & \sigma_h(z) & 0 \\ 0 & 0 & \sigma_v(z) \end{pmatrix}, \tag{6}$$

where $\sigma_h > 0$ is the conductivity of the media along the x and y directions, and $\sigma_v > 0$ is the conductivity along z direction. Our formulation allows for parameter variations in the parameters along the z-axis. Analogously, $\boldsymbol{\varepsilon}(z)$ and $\boldsymbol{\mu}(z)$ are considered to be transversely isotropic tensors.

Since material properties are uniform in the xy-plane, it is convenient to use a Hankel transform to represent the magnetic field along x and y directions.

3.1. Hankel transform

We consider $\widehat{\boldsymbol{H}}$ to be the 2D Fourier transform of $\boldsymbol{\mathcal{H}}$ along x and y directions, where the material properties are homogeneous. We have:

$$\boldsymbol{\mathcal{H}}(\boldsymbol{x}, z) = \frac{1}{4\pi^2} \int_{-\infty}^{+\infty} \int_{-\infty}^{+\infty} \widehat{\boldsymbol{H}}(\boldsymbol{k}, z) e^{i\boldsymbol{k}\cdot\boldsymbol{x}} d\boldsymbol{k}, \tag{7}$$

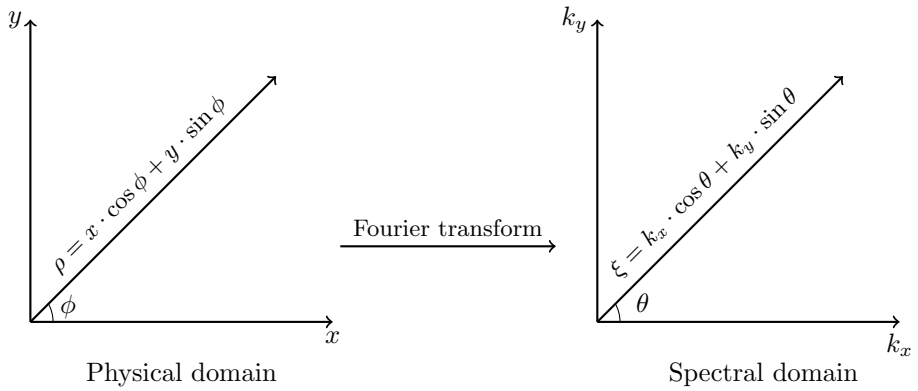

Figure 1: Cartesian and cylindrical systems of coordinates.

where $\boldsymbol{x} = (x, y)$ and $\boldsymbol{k} = (k_x, k_y)$ (see Figure 1). We switch from the Cartesian system of coordinates to a cylindrical one according to the following transformations:

$$\begin{aligned} &x = \rho \cdot \cos\phi, \;\; y = \rho \cdot \sin\phi, \\ &k_x = \xi \cdot \cos\theta, \;\; k_y = \xi \cdot \sin\theta. \end{aligned} \tag{8}$$

Substituting (8) into (7) and applying the change of coordinates under the integral signs, we obtain:

$$\boldsymbol{\mathcal{H}}(\boldsymbol{\rho}) = \frac{1}{4\pi^2} \int_0^{+\infty} \int_0^{2\pi} \widehat{\boldsymbol{H}}(\xi, \theta, z) e^{i\xi\rho(\cos\theta\cos\phi + \sin\theta\sin\phi)} d\theta\xi d\xi, \tag{9}$$

where $\boldsymbol{\rho} = (\rho, \phi, z)$. Using the trigonometric identity:

$$\cos(\phi - \theta) = \cos\theta\cos\phi + \sin\theta\sin\phi, \tag{10}$$

we obtain:

$$\boldsymbol{\mathcal{H}}(\boldsymbol{\rho}) = \frac{1}{4\pi^2} \int_0^{+\infty} \int_0^{2\pi} \widehat{\boldsymbol{H}}(\xi, \theta, z) e^{i\xi\rho\cos(\phi-\theta)} d\theta\xi d\xi. \tag{11}$$

We now use the following relation between exponentials and Bessel functions:

$$e^{i\xi\rho\cos(\phi-\theta)} = \sum_{m=-\infty}^{\infty} i^m J_m(\xi\rho) e^{-im(\phi-\theta)} \tag{12}$$

to obtain

$$\boldsymbol{\mathcal{H}}(\boldsymbol{\rho}) = \frac{1}{2\pi} \sum_{m=-\infty}^{\infty} \int_0^{+\infty} \boldsymbol{H}^m(\xi, z) J_m(\xi\rho) e^{-im\phi} \xi d\xi, \tag{13}$$

where

$$\boldsymbol{H}^m(\xi, z) = \frac{1}{2\pi} \int_0^{2\pi} \widehat{\boldsymbol{H}}(\xi, \theta, z) i^m e^{im\theta} d\theta. \tag{14}$$

We compute the cylindrical components of the magnetic field as follows:

$$\begin{aligned} H_\rho^m &= \cos\phi \cdot H_x^m + \sin\phi \cdot H_y^m \\ &= e^{i\phi}\left(\frac{H_x^m - iH_y^m}{2}\right) + e^{-i\phi}\left(\frac{H_x^m + iH_y^m}{2}\right) \\ &= e^{i\phi} H_+^m + e^{-i\phi} H_-^m, \end{aligned} \tag{15}$$

where

$$\begin{aligned} H_+^m &= \frac{H_x^m - iH_y^m}{2}, \\ H_-^m &= \frac{H_x^m + iH_y^m}{2}. \end{aligned} \tag{16}$$

Similarly for $\mathcal{H}_\phi$, we have:

$$H_\phi^m = -\sin\phi \cdot H_x^m + \cos\phi \cdot H_y^m = i\left(e^{i\phi} H_+^m - e^{-i\phi} H_-^m\right). \tag{17}$$

By substituting (15) and (17) into (13), the Hankel representation of the magnetic field becomes:

$$\begin{aligned} \mathcal{H}_\rho(\boldsymbol{\rho}) &= \frac{1}{2\pi} \sum_{m=-\infty}^{+\infty} e^{-im\phi} \int_0^{+\infty} \Big(H_+^m(\xi, z) J_{m+1}(\xi\rho) + H_-^m(\xi, z) J_{m-1}(\xi\rho)\Big) \xi d\xi, \\ \mathcal{H}_\phi(\boldsymbol{\rho}) &= \frac{i}{2\pi} \sum_{m=-\infty}^{+\infty} e^{-im\phi} \int_0^{+\infty} \Big(H_+^m(\xi, z) J_{m+1}(\xi\rho) - H_-^m(\xi, z) J_{m-1}(\xi\rho)\Big) \xi d\xi, \\ \mathcal{H}_z(\boldsymbol{\rho}) &= \frac{1}{2\pi} \sum_{m=-\infty}^{+\infty} e^{-im\phi} \int_0^{+\infty} H_z^m(\xi, z) J_m(\xi\rho) \xi d\xi. \end{aligned} \tag{18}$$

The curl of the magnetic field in cylindrical coordinates is:

$$\begin{aligned} \nabla \times \boldsymbol{\mathcal{H}} = &\left(\frac{1}{\rho}\frac{\partial \mathcal{H}_z}{\partial \phi} - \frac{\partial \mathcal{H}_\phi}{\partial z}\right) \hat{\boldsymbol{\rho}} + \left(\frac{\partial \mathcal{H}_\rho}{\partial z} - \frac{\partial \mathcal{H}_z}{\partial \rho}\right) \hat{\boldsymbol{\phi}} \\ &+ \frac{1}{\rho}\left(\mathcal{H}_\phi + \rho\frac{\partial \mathcal{H}_\phi}{\partial \rho} - \frac{\partial \mathcal{H}_\rho}{\partial \phi}\right) \hat{\boldsymbol{z}}. \end{aligned} \tag{19}$$

By substituting (18) into (19), the first component of the curl becomes:

$$(\nabla \times \boldsymbol{\mathcal{H}})_\rho = \frac{-i}{2\pi} \sum_{m=-\infty}^{+\infty} e^{-im\phi} \int_\xi \Bigg(\frac{m}{\rho} H_z^m(\xi, z) J_m(\xi\rho) + \frac{\partial H_+^m(\xi, z)}{\partial z} J_{m+1}(\xi\rho) - \frac{\partial H_-^m(\xi, z)}{\partial z} J_{m-1}(\xi\rho) \Bigg) \xi d\xi. \tag{20}$$

By using the property of Bessel functions given by Equation (92) of Appendix A, we obtain:

$$(\nabla \times \boldsymbol{\mathcal{H}})_\rho = \frac{-i}{2\pi} \sum_{m=-\infty}^{+\infty} e^{-im\phi} \int_\xi \Bigg[H_z^m(\xi, z) \left(\xi J_{m-1}(\xi\rho) - \xi \frac{\partial J_m(\xi\rho)}{\partial (\xi\rho)} \right) + \frac{\partial H_+^m(\xi, z)}{\partial z} J_{m+1}(\xi\rho) - \frac{\partial H_-^m(\xi, z)}{\partial z} J_{m-1}(\xi\rho) \Bigg] \xi d\xi. \tag{21}$$

Using the formula of the derivative of the Bessel function given by Equation (90) of Appendix A, we have:

$$(\nabla \times \boldsymbol{\mathcal{H}})_\rho = \frac{-i}{2\pi} \sum_{m=-\infty}^{+\infty} e^{-im\phi} \int_\xi \Bigg[H_z^m(\xi, z) \Bigg(\xi J_{m-1}(\xi\rho) - \frac{\xi}{2} J_{m-1}(\xi\rho) + \frac{\xi}{2} J_{m+1}(\xi\rho) \Bigg) + \frac{\partial H_+^m(\xi, z)}{\partial z} J_{m+1}(\xi\rho) - \frac{\partial H_-^m(\xi, z)}{\partial z} J_{m-1}(\xi\rho) \Bigg] \xi d\xi. \tag{22}$$

For an arbitrary function $\mathbf{g}(\xi, z) = (g_-(\xi, z), g_+(\xi, z), g_z(\xi, z))$ in the spectral domain, we introduce the following notation to simplify computations:

$$\begin{aligned} \mathit{\Pi}_+^\xi (\mathbf{g}(\xi, z)) &= \frac{\partial g_+(\xi, z)}{\partial z} + \frac{\xi}{2} g_z(\xi, z), \\ \mathit{\Pi}_-^\xi (\mathbf{g}(\xi, z)) &= \frac{\partial g_-(\xi, z)}{\partial z} - \frac{\xi}{2} g_z(\xi, z), \\ \mathit{\Pi}_z^\xi (\mathbf{g}(\xi, z)) &= \xi \left(g_-(\xi, z) + g_+(\xi, z) \right). \end{aligned} \tag{23}$$

Using (23), we obtain:

$$(\nabla \times \boldsymbol{\mathcal{H}})_\rho = -\frac{i}{2\pi} \sum_{m=-\infty}^{+\infty} e^{-im\phi} \int_\xi \Big(\mathit{\Pi}_+^\xi (\mathbf{H}^m(\xi, z)) J_{m+1}(\xi\rho) - \mathit{\Pi}_-^\xi (\mathbf{H}^m(\xi, z)) J_{m-1}(\xi\rho) \Big) \xi d\xi. \tag{24}$$

For the second component of (19), using (18), we have:

$$(\nabla \times \boldsymbol{\mathcal{H}})_{\phi} = \frac{1}{2\pi} \sum_{m=-\infty}^{+\infty} e^{-im\phi} \int_{\xi} \Bigg[\Bigg(\frac{\partial H_{+}^{m}(\xi, z)}{\partial z} J_{m+1}(\xi\rho) + \frac{\partial H_{-}^{m}(\xi, z)}{\partial z} J_{m-1}(\xi\rho) \Bigg) - H_{z}^{m}(\xi, z) \frac{\partial J_{m+1}(\xi\rho)}{\partial (\xi\rho)} \xi \Bigg] \xi d\xi. \tag{25}$$

Using the property of the Bessel functions given by Equation (90) of Appendix A and (23), we obtain:

$$(\nabla \times \boldsymbol{\mathcal{H}})_{\phi} = \frac{1}{2\pi} \sum_{m=-\infty}^{+\infty} e^{-im\phi} \int_{\xi} \Big(\Pi_{+}^{\xi} \left(\mathbf{H}^{m}(\xi, z) \right) J_{m+1}(\xi\rho) + \Pi_{-}^{\xi} \left(\mathbf{H}^{m}(\xi, z) \right) J_{m-1}(\xi\rho) \Big) \xi d\xi. \tag{26}$$

The third component of (19), becomes after using (18):

$$\begin{aligned} (\nabla \times \boldsymbol{\mathcal{H}})_{z} = \frac{i}{2\pi} \sum_{m=-\infty}^{+\infty} e^{-im\phi} \cdot \int_{\xi} \Bigg[& \Bigg(\frac{J_{m+1}(\xi\rho)}{\rho} + \xi \frac{\partial J_{m+1}(\xi\rho)}{\partial (\xi\rho)} \\ & + \frac{m}{\rho} J_{m+1}(\xi\rho) \Bigg) H_{+}^{m}(\xi, z) \\ & - \Bigg(\frac{J_{m-1}(\xi\rho)}{\rho} + \xi \frac{\partial J_{m-1}(\xi\rho)}{\partial (\xi\rho)} \\ & - \frac{m}{\rho} J_{m-1}(\xi\rho) \Bigg) H_{-}^{m}(\xi, z) \Bigg] \xi d\xi. \end{aligned} \tag{27}$$

For the derivative of J_{m+1}, we use Equation (92) of Appendix A, and for the derivative of J_{m-1}, we use Equation (90) of the same appendix. Then,

$$\begin{aligned} (\nabla \times \boldsymbol{\mathcal{H}})_{z} = \frac{i}{2\pi} \sum_{m=-\infty}^{+\infty} e^{-im\phi} \int_{\xi} \Bigg[& \Bigg(\frac{J_{m+1}(\xi\rho)}{\rho} + \xi J_{m}(\xi\rho) \\ & - \frac{m+1}{\rho} J_{m+1}(\xi\rho) + \frac{m}{\rho} J_{m+1}(\xi\rho) \Bigg) H_{+}^{m}(\xi, z) \\ & - \Bigg(\frac{J_{m-1}(\xi\rho)}{\rho} + \frac{\xi}{2} J_{m-2}(\xi\rho) \\ & - \frac{\xi}{2} J_{m}(\xi\rho) - \frac{m}{\rho} J_{m-1}(\xi\rho) \Bigg) H_{-}^{m}(\xi, z) \Bigg] \xi d\xi. \end{aligned} \tag{28}$$

We use Equation (87) of Appendix A to simplify J_{m-2}. As a result, we obtain:

$$(\nabla \times \boldsymbol{\mathcal{H}})_z = \frac{i}{2\pi} \sum_{m=-\infty}^{+\infty} e^{-im\phi} \int_\xi \Pi_z^\xi \left(\mathbf{H}^m(\xi, z)\right) J_m(\xi\rho)\xi d\xi. \tag{29}$$

3.2. Hankel Finite Element (HFE) full field formulation

L^2-orthogonality holds for Bessel functions of with the same order (see Equation (89) of Appendix A). Hence, in order to simplify the terms of the variational formulation containing Bessel functions, we introduce the following matrix:

$$Q = \frac{1}{\sqrt{2}} \begin{pmatrix} 1 & i & 0 \\ i & 1 & 0 \\ 0 & 0 & \sqrt{2} \end{pmatrix}. \tag{30}$$

Q is a unitary matrix, since:

$$QQ^* = Q^*Q = I.$$

Hence, the change of coordinates implied by Q preserves the inner product. In particular, for arbitrary vector-valued functions $\mathbf{U}$ and $\mathbf{V}$, we have:

$$\mathbf{V}^*\mathbf{U} = (Q\mathbf{V})^*(Q\mathbf{U}).$$

By using the above matrix, we obtain the following equalities:

$$\begin{aligned}
\left(Q\tilde{\boldsymbol{\sigma}}^{-1}(z)\nabla \times \boldsymbol{\mathcal{H}}\right)_\rho &= \frac{i}{\sqrt{2}\pi} \sum_{m=-\infty}^{+\infty} e^{-im\phi} \int_0^{+\infty} \tilde{\sigma}_h^{-1}(z) \\
&\qquad \cdot \Pi_-^\xi \left(\mathbf{H}^m(\xi, z)\right) J_{m-1}(\xi\rho)\xi d\xi, \\
\left(Q\tilde{\boldsymbol{\sigma}}^{-1}(z)\nabla \times \boldsymbol{\mathcal{H}}\right)_\phi &= \frac{1}{\sqrt{2}\pi} \sum_{m=-\infty}^{+\infty} e^{-im\phi} \int_0^{+\infty} \tilde{\sigma}_h^{-1}(z) \\
&\qquad \cdot \Pi_+^\xi \left(\mathbf{H}^m(\xi, z)\right) J_{m+1}(\xi\rho)\xi d\xi, \\
\left(Q\tilde{\boldsymbol{\sigma}}^{-1}(z)\nabla \times \boldsymbol{\mathcal{H}}\right)_z &= \frac{i}{2\pi} \sum_{m=-\infty}^{+\infty} e^{-im\phi} \int_0^{+\infty} \tilde{\sigma}_v^{-1}(z) \\
&\qquad \cdot \Pi_z^\xi \left(\mathbf{H}^m(\xi, z)\right) J_m(\xi\rho)\xi d\xi,
\end{aligned} \tag{31}$$

where $\tilde{\sigma}_h = \sigma_h - i\omega\varepsilon_h$ and $\tilde{\sigma}_v = \sigma_v - i\omega\varepsilon_v$. For the L^2 terms, we obtain:

$$\begin{aligned}
\left(Q\boldsymbol{\mathcal{H}}\right)_\rho &= \frac{1}{\sqrt{2}\pi}\sum_{m=-\infty}^{+\infty} e^{-im\phi}\int_0^{+\infty} H_-^m(\xi,z)J_{m-1}(\xi\rho)\xi d\xi,\\
\left(Q\boldsymbol{\mathcal{H}}\right)_\phi &= \frac{i}{\sqrt{2}\pi}\sum_{m=-\infty}^{+\infty} e^{-im\phi}\int_0^{+\infty} H_+^m(\xi,z)J_{m+1}(\xi\rho)\xi d\xi,\\
\left(Q\boldsymbol{\mathcal{H}}\right)_z &= \frac{1}{2\pi}\sum_{m=-\infty}^{+\infty} e^{-im\phi}\int_0^{+\infty} H_z^m(\xi,z)J_m(\xi\rho)\xi d\xi.
\end{aligned} \tag{32}$$

For a specific Hankel mode $\xi_q > 0$ and an exponential order t, we select a mono-modal test function of the form:

$$\boldsymbol{\mathcal{F}}^{q,t}(\boldsymbol{\rho}) = \mathcal{F}_\rho^{q,t}(\boldsymbol{\rho})\hat{\boldsymbol{\rho}} + \mathcal{F}_\phi^{q,t}(\boldsymbol{\rho})\hat{\boldsymbol{\phi}} + \mathcal{F}_z^{q,t}(\boldsymbol{\rho})\hat{\mathbf{z}}, \tag{33}$$

where:

$$\begin{aligned}
\mathcal{F}_\rho^{q,t}(\boldsymbol{\rho}) &= e^{-it\phi}\Big(F_+^t(\xi_q,z)J_{t+1}(\xi_q\rho) + F_-^t(\xi_q,z)J_{t-1}(\xi_q\rho)\Big),\\
\mathcal{F}_\phi^{q,t}(\boldsymbol{\rho}) &= ie^{-it\phi}\Big(F_+^t(\xi_q,z)J_{t+1}(\xi_q\rho) - F_-^t(\xi_q,z)J_{t-1}(\xi_q\rho)\Big),\\
\mathcal{F}_z^{q,t}(\boldsymbol{\rho}) &= e^{-it\phi}F_z^t(\xi_q,z)J_t(\xi_q\rho).
\end{aligned} \tag{34}$$

Using (31) and the test functions defined in (34), we have:

$$\begin{aligned}
&\int_{z,\phi,\rho}\left(Q\nabla\times\boldsymbol{\mathcal{F}}^{q,t}\right)_\rho^*\left(Q\tilde{\boldsymbol{\sigma}}^{-1}(z)\nabla\times\boldsymbol{\mathcal{H}}\right)_\rho\rho d\rho d\phi dz\\
&\qquad= \frac{1}{\pi}\int_z\Bigg(\sum_{m=-\infty}^{+\infty}\int_{\xi,\phi,\rho} e^{i(t-m)\phi}\\
&\qquad\qquad\cdot\left(\Pi_-^{\xi_q}\left(\mathbf{F}^t\right)\right)^*\tilde{\sigma}_h^{-1}(z)\Pi_-^{\xi}(\mathbf{H}^m)\\
&\qquad\qquad\cdot J_{t-1}(\xi_q\rho)J_{m-1}(\xi\rho)\rho d\rho d\phi\xi d\xi\Bigg)dz,
\end{aligned} \tag{35}$$

where $\mathbf{F}^t = (F_+^t, F_-^t, F_z^t)$. Separating the integrals according to each variable and using the L^2-orthogonality property of exponential functions, we have:

$$\begin{aligned}
&\int_{z,\phi,\rho}\left(Q\nabla\times\boldsymbol{\mathcal{F}}^{q,t}\right)_\rho^*\left(Q\tilde{\boldsymbol{\sigma}}^{-1}(z)\nabla\times\boldsymbol{\mathcal{H}}\right)_\rho\rho d\rho d\phi dz\\
&\qquad= 2\int_z\Bigg[\int_\xi\Bigg(\left(\Pi_-^{\xi_q}\left(\mathbf{F}^t\right)\right)^*\tilde{\sigma}_h^{-1}(z)\Pi_-^{\xi}(\mathbf{H}^t)\\
&\qquad\qquad\cdot\int_\rho J_{t-1}(\xi_q\rho)J_{t-1}(\xi\rho)\rho d\rho\Bigg)\xi d\xi\Bigg]dz.
\end{aligned} \tag{36}$$

By the orthogonality property of the Bessel functions given by Equation (89) of Appendix A, we obtain:

$$\begin{aligned}\int_{z,\phi,\rho} \left(Q\nabla\times\boldsymbol{\mathcal{F}}^{q,t}\right)_{\rho}^{*} \left(Q\tilde{\boldsymbol{\sigma}}^{-1}(z)\nabla\times\boldsymbol{\mathcal{H}}\right)_{\rho} \rho d\rho d\phi dz \\ = 2\int_{z} \left(\Pi_{-}^{\xi_q}\left(\mathbf{F}^{t}\right)\right)^{*} \tilde{\sigma}_{h}^{-1}(z)\Pi_{-}^{\xi_q}(\mathbf{H}^{t})dz.\end{aligned} \tag{37}$$

Similarly, for the other components of the curl, we have:

$$\begin{aligned}\int_{z,\phi,\rho} \left(Q\nabla\times\boldsymbol{\mathcal{F}}^{q,t}\right)_{\phi}^{*} \left(Q\tilde{\boldsymbol{\sigma}}^{-1}(z)\nabla\times\boldsymbol{\mathcal{H}}\right)_{\phi} \rho d\rho d\phi dz \\ = 2\int_{z} \left(\Pi_{+}^{\xi_q}\left(\mathbf{F}^{t}\right)\right)^{*} \tilde{\sigma}_{h}^{-1}(z)\Pi_{+}^{\xi_q}(\mathbf{H}^{t})dz,\end{aligned} \tag{38}$$

$$\begin{aligned}\int_{z,\phi,\rho} \left(Q\nabla\times\boldsymbol{\mathcal{F}}^{q,t}\right)_{z}^{*} \left(Q\tilde{\boldsymbol{\sigma}}^{-1}(z)\nabla\times\boldsymbol{\mathcal{H}}\right)_{z} \rho d\rho d\phi dz \\ = \int_{z} \left(\Pi_{z}^{\xi_q}\left(\mathbf{F}^{t}\right)\right)^{*} \tilde{\sigma}_{v}^{-1}(z)\Pi_{z}^{\xi_q}\left(\mathbf{H}^{t}\right)dz.\end{aligned} \tag{39}$$

For the L^2 terms, using (32) and the test functions defined in (34), and using L^2-orthogonality property of exponentials and orthogonality property of the Bessel functions given by (89) of Appendix A, we obtain:

$$\begin{aligned}\int_{z,\phi,\rho} \left(Q\boldsymbol{\mathcal{F}}^{q,t}\right)_{\rho}^{*} \left(Q\boldsymbol{\mu}\boldsymbol{\mathcal{H}}\right)_{\rho} \rho d\rho d\phi dz &= 2\int_{z} \left(F_{-}^{t}(\xi_q,z)\right)^{*} \mu_h(z)H_{-}^{t}(\xi_q,z)dz, \\ \int_{z,\phi,\rho} \left(Q\boldsymbol{\mathcal{F}}^{q,t}\right)_{\phi}^{*} \left(Q\boldsymbol{\mu}\boldsymbol{\mathcal{H}}\right)_{\phi} \rho d\rho d\phi dz &= 2\int_{z} \left(F_{+}^{t}(\xi_q,z)\right)^{*} \mu_h(z)H_{+}^{t}(\xi_q,z)dz, \\ \int_{z,\phi,\rho} \left(Q\boldsymbol{\mathcal{F}}^{q,t}\right)_{z}^{*} \left(Q\boldsymbol{\mu}\boldsymbol{\mathcal{H}}\right)_{z} \rho d\rho d\phi dz &= \int_{z} \left(F_{z}^{t}(\xi_q,z)\right)^{*} \mu_v(z)H_{z}^{t}(\xi_q,z)dz.\end{aligned} \tag{40}$$

Using (37), (38), (39) and (40), for each Hankel mode $\xi_q > 0$ and exponential order t, the stiffness matrix becomes:

$$b(\boldsymbol{\mathcal{F}}^{q,t},\boldsymbol{\mathcal{H}}) = b(\mathbf{F}^{t},\mathbf{H}^{t}) = b_1(\mathbf{F}^{t},\mathbf{H}^{t}) - b_2(\mathbf{F}^{t},\mathbf{H}^{t}), \tag{41}$$

where

$$\begin{aligned}b_1(\mathbf{F}^{t},\mathbf{H}^{t}) =& 2\langle\Pi_{-}^{\xi_q}\left(\mathbf{F}^{t}\right),\tilde{\sigma}_{h}^{-1}\Pi_{-}^{\xi_q}\left(\mathbf{H}^{t}\right)\rangle_{L^2} + 2\langle\Pi_{+}^{\xi_q}\left(\mathbf{F}^{t}\right),\tilde{\sigma}_{h}^{-1}\Pi_{+}^{\xi_q}\left(\mathbf{H}^{t}\right)\rangle_{L^2} \\ &+ \langle\Pi_{z}^{\xi_q}\left(\mathbf{F}^{t}\right),\tilde{\sigma}_{v}^{-1}\Pi_{z}^{\xi_q}\left(\mathbf{H}^{t}\right)\rangle_{L^2}, \\ b_2(\mathbf{F}^{t},\mathbf{H}^{t}) =& i\omega\left(2\langle F_{-}^{t},\mu_h H_{-}^{t}\rangle_{L^2} + 2\langle F_{+}^{t},\mu_h H_{+}^{t}\rangle_{L^2} + \langle F_{z}^{t},\mu_v H_{z}^{t}\rangle_{L^2}\right).\end{aligned} \tag{42}$$

Symbol $< ., . >_{L^2}$ represents the L^2 inner product given by:

$$\langle f, g \rangle_{L^2} = \int_z f^* g dz.$$

A sufficient condition to guarantee that the above integrals are finite is to require $\mathbf{H}^t, \mathbf{F}^t \in V(\mathbb{R})$, where $V(\mathbb{R}) = H^1(\mathbb{R}) \times H^1(\mathbb{R}) \times L^2(\mathbb{R})$, and

$$H^1(\mathbb{R}) = \{v \in L^2(\mathbb{R}) : \frac{\partial v}{\partial z} \in L^2(\mathbb{R})\}. \tag{43}$$

In (43), the weak derivative of the function is considered.

3.2.1. Load vector

In 1D layered medium, we consider $(0, 0, z_{Tx})$ to be the general representation of a point source location. We use the following identities to describe the right-hand-side vector in cylindrical coordinates:

$$\begin{aligned}
\hat{\boldsymbol{x}} &= \cos(\phi)\hat{\boldsymbol{\rho}} - \sin(\phi)\hat{\boldsymbol{\phi}} = \frac{e^{-i\phi}}{2}(\hat{\boldsymbol{\rho}} - i\hat{\boldsymbol{\phi}}) + \frac{e^{i\phi}}{2}(\hat{\boldsymbol{\rho}} + i\hat{\boldsymbol{\phi}}), \\
\hat{\boldsymbol{y}} &= \sin(\phi)\hat{\boldsymbol{\rho}} + \cos(\phi)\hat{\boldsymbol{\phi}} = \frac{e^{-i\phi}}{2}(i\hat{\boldsymbol{\rho}} + \hat{\boldsymbol{\phi}}) - \frac{e^{i\phi}}{2}(i\hat{\boldsymbol{\rho}} - \hat{\boldsymbol{\phi}}), \\
\hat{\boldsymbol{z}} &= \hat{\boldsymbol{z}},
\end{aligned} \tag{44}$$

where $\hat{\boldsymbol{x}}$, $\hat{\boldsymbol{y}}$ and $\hat{\boldsymbol{z}}$ are the unitary vectors in Cartesian coordinates. The right-hand-side of (3) in cylindrical coordinates for a z-oriented point source is:

$$\mathbf{R}_z = i\omega\mu_v(z)\frac{1}{2\pi\rho}\delta(\rho, 0)\delta(z, z_{Tx})\hat{\boldsymbol{z}},$$

where δ is the Dirac delta distribution. We consider l to be the right-hand-side of (5). Using $\boldsymbol{\mathcal{F}}^{q,t}$ as our test function and separating the integrals according to each variable, we obtain:

$$\begin{aligned}
l(\mathbf{F}^t) = &\frac{i\omega}{2\pi}\int_{\phi=0}^{2\pi} e^{it\phi}d\phi \int_{\rho=0}^{+\infty} J_t(\xi_q\rho)\delta(\rho, 0)\rho d\rho \\
&\cdot \int_{z=-\infty}^{+\infty} \mu_v(z)\left(F_z^t(\xi_q, z)\right)^* \delta(z, z_{Tx})dz.
\end{aligned} \tag{45}$$

By L^2-orthogonality of the exponentials, the load vector is non-zero when $t = 0$. Since $J_0(0) = 1$, for a z-oriented point source, the right-hand-side becomes:

$$l(\mathbf{F}^0) = i\omega\mu_v(z_{Tx})\left(F_z^0(\xi_q, z_{Tx})\right)^*. \tag{46}$$

Hence, we obtain the field by solving the following variational formulation:

$$b(\mathbf{F}^0, \mathbf{H}^0) = l(\mathbf{F}^0), \text{ for all } \mathbf{F}^0 \in V(\mathbb{R}). \tag{47}$$

Lets consider $\mathbf{R}_x$ and $\mathbf{R}_y$ to be the right-hand-sides of (3) for x and y-oriented sources, respectively. By using (44), we obtain:

$$\begin{aligned}
\mathbf{R}_x &= \lim_{\rho_{Tx}\to 0^+} \frac{i\omega\mu_h(z)}{2\pi\rho}\delta(\rho,\rho_{Tx})\delta(z,z_{Tx})\left(\frac{e^{-i\phi}}{2}(\hat{\boldsymbol{\rho}}-i\hat{\boldsymbol{\phi}})+\frac{e^{i\phi}}{2}(\hat{\boldsymbol{\rho}}+i\hat{\boldsymbol{\phi}})\right),\\
\mathbf{R}_y &= \lim_{\rho_{Tx}\to 0^+} \frac{i\omega\mu_h(z)}{2\pi\rho}\delta(\rho,\rho_{Tx})\delta(z,z_{Tx})\left(\frac{e^{-i\phi}}{2}(i\hat{\boldsymbol{\rho}}+\hat{\boldsymbol{\phi}})-\frac{e^{i\phi}}{2}(i\hat{\boldsymbol{\rho}}-\hat{\boldsymbol{\phi}})\right).
\end{aligned} \tag{48}$$

Similarly to (46), the right-hand-side of the variational formulation is non-zero only when $t=-1,1$. For those values of t, and for each Hankel mode, we have:

$$b(\mathbf{F}^t, \mathbf{H}^t) = \lim_{\rho_{Tx}\to 0+} l(\mathbf{F}^t), \text{ for all } \mathbf{F}^t \in V(\mathbb{R}), \tag{49}$$

where,

$$\begin{aligned}
l(\mathbf{F}^t) =& i\omega\mu_h(z_{Tx})\Bigg[\frac{F_+^t(\xi_q,z_{Tx})}{2}J_{t+1}(\xi_q\rho_{Tx})+\frac{F_-^t(\xi_q,z_{Tx})}{2}J_{t-1}(\xi_q\rho_{Tx})\\
&-t\left(\frac{F_+^t(\xi_q,z_{Tx})}{2}J_{t+1}(\xi_q\rho_{Tx})-\frac{F_-^t(\xi_q,z_{Tx})}{2}J_{t-1}(\xi_q\rho_{Tx})\right)\Bigg]^*\\
=& i\omega\mu_h(z_{Tx})J_0(\xi_q\rho_{Tx})\begin{cases}\left(F_+^t(\xi_q,z_{Tx})\right)^*, & t=-1,\\ \left(F_-^t(\xi_q,z_{Tx})\right)^*, & t=1.\end{cases}
\end{aligned} \tag{50}$$

Based on (18), we define the following notation:

$$\begin{aligned}
\mathcal{H}_\rho^t(\boldsymbol{\rho}) &= \frac{1}{2\pi}e^{-it\phi}\int_{\xi=0}^{+\infty}\Big(H_+^t(\xi,z)J_{t+1}(\xi\rho)+H_-^t(\xi,z)J_{t-1}(\xi\rho)\Big)\xi d\xi,\\
\mathcal{H}_\phi^t(\boldsymbol{\rho}) &= \frac{i}{2\pi}e^{-it\phi}\int_{\xi=0}^{+\infty}\Big(H_+^t(\xi,z)J_{t+1}(\xi\rho)-H_-^t(\xi,z)J_{t-1}(\xi\rho)\Big)\xi d\xi,\\
\mathcal{H}_z^t(\boldsymbol{\rho}) &= \frac{1}{2\pi}e^{-it\phi}\int_{\xi=0}^{+\infty}H_z^t(\xi,z)J_t(\xi\rho)\xi d\xi.
\end{aligned} \tag{51}$$

We have $\boldsymbol{\mathcal{H}}^t = (\mathcal{H}_\rho^t, \mathcal{H}_\phi^t, \mathcal{H}_z^t)$. Therefore, the magnetic field for the x-oriented source is:

$$\boldsymbol{\mathcal{H}} = \boldsymbol{\mathcal{H}}^1 + \boldsymbol{\mathcal{H}}^{-1}. \tag{52}$$

For a y-oriented source, the field is computed as:

$$\boldsymbol{\mathcal{H}} = i\boldsymbol{\mathcal{H}}^1 - i\boldsymbol{\mathcal{H}}^{-1}. \tag{53}$$

4. Multi-scale Hankel Finite Element Method (Ms-HFEM)

We now describe our multi-scale FE method in the Hankel domain. In order to make the computational problem tractable, we truncate our domain along the z direction. We consider $\Omega_z = (z_0, z_N)$ to be our problem domain along z direction and we have $-\infty < z_0$ and $z_N < \infty$. Moreover, we consider our solution to satisfy a zero Dirichlet boundary condition at both ends, since the waves amplitude rapidly decreases as we move away from the source. Thus, we have $\mathbf{H}^m, \mathbf{F}^m \in V_0(\Omega_z)$, where $V_0(\Omega_z) = H_0^1(\Omega_z) \times H_0^1(\Omega_z) \times L^2(\Omega_z)$, with:

$$H_0^1(\Omega_z) = \{v \in H^1(\Omega_z), v(z_i) = 0 \text{ for } z_i \in \partial\Omega_z\}. \tag{54}$$

In the following, for simplicity, we shall remove symbols ξ_q and t from the notation. For each Hankel mode, we need to solve three problems associated with $t = -1, 0, 1$. The curl operator is the one defined in (24), (26) and (29). Similarly, $\mathit{\Pi}_+$, $\mathit{\Pi}_-$, and $\mathit{\Pi}_z$ are the symbols defined in Equation (23), and l is the right-hand-side of the variational formulation described in Equations (46) and (50) for $t = -1, 0, 1$. Our multi-scale approach consists of the following steps for each Hankel mode:

1. **Divide our domain into a finite number of sub-domains**. We consider $z_0, z_1, z_2, \cdots, z_{N-1}, z_N$, where $z_1, z_2, \cdots, z_{N-1}$ are arbitrary real numbers and $z_0 < z_1 < \cdots < z_N$ (see Figure 2). We call them decomposition points. We define each sub-domain as $\Omega_i = (z_{i-1}, z_i)$, and we have:

$$\overline{\Omega_z} = \bigcup_{i=1}^{N} \overline{\Omega_i}. \tag{55}$$

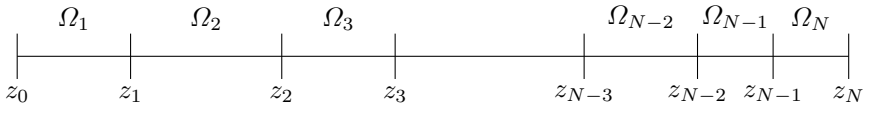

Figure 2: Selected decomposition points $z_1, \cdots, z_{N-1}$ in the domain (z_0, z_N). $\Omega_1, \Omega_2, \cdots, \Omega_N$ are the sub-domains associated to the decomposition points.

2. **Divide our magnetic field into primary and secondary fields**. For each Hankel mode, we decompose our magnetic field as follows:

$$\mathbf{H}(z) = \mathbf{H}^P(z) + \mathbf{H}^S(z), \tag{56}$$

where $\mathbf{H}^P$ and $\mathbf{H}^S$ are primary and secondary fields, respectively.

3. **Find a local primary field**. Lets assume that $z_{Tx} \in \Omega_p$ (see Figure 3). We define our local primary field $\mathbf{H}^P \in V_0(\Omega_p)$ as the one that satisfies:

$$b(\mathbf{F}, \mathbf{H}^P) = l(\mathbf{F}), \ \mathbf{F} \in V_0(\Omega_p). \tag{57}$$

Extending the local primary field to the entire domain with zero, we have $\mathbf{H}^P \in V_0(\Omega_z)$. The local primary field has a discontinuous flux at z_{p-1} and z_p. For the special case when the source is located at one decomposition point, we consider $z_{Tx} = z'_p$, where

$$z'_p = \begin{cases} z_{Tx} + 10^{-5}\text{meters} & z_{Tx} = z_{p-1}, \\ z_{Tx} - 10^{-5}\text{meters} & z_{Tx} = z_p. \end{cases} \tag{58}$$

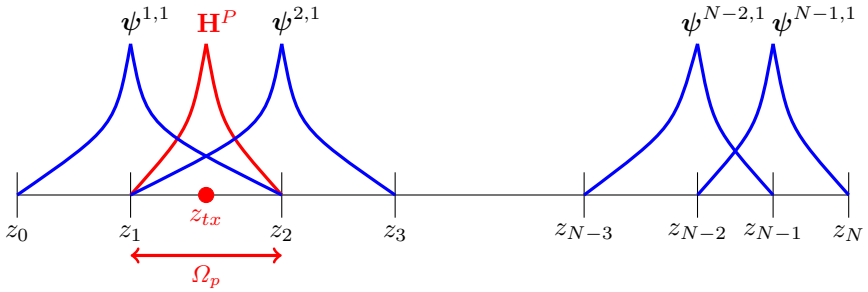

Figure 3: Multi-scale basis functions $\boldsymbol{\psi}^{1,1}, \boldsymbol{\psi}^{2,1}, \cdots, \boldsymbol{\psi}^{N-1,1}$ and local primary field $\mathbf{H}^P$. Ω_p is the domain of the local primary field.

4. **Solve** $(N-1)$ **pairs of local problems**. We consider $\Omega_i^M = \Omega_i \cup \Omega_{i+1} \cup \{z_i\}$, $i = 1, \cdots, (N-1)$. For each sub-domain Ω_i^M, we solve a pair of local problems which correspond to a discontinuous flux at the node $z = z_i$. Specifically, the flux of the first local problem has a jump equal to $\mathbf{1}_1 = (1, 0, 0)$, and the

flux of the second local problem has a jump equal to $\mathbf{1}_2 = (0, 1, 0)$. The local functions $\boldsymbol{\psi}^{i,k} \in V_0(\Omega_i^M)$ solve the following variational problems:

$$b(\mathbf{F}, \boldsymbol{\psi}^{i,k}) = l^{M,k}(\mathbf{F}),\ \mathbf{F} \in V_0(\Omega_i^M),\ i = 1, \cdots, (N-1),\ k = 1, 2, \tag{59}$$

where $\boldsymbol{\psi}^{i,k}(z) = (\psi_-^{i,k}(z), \psi_+^{i,k}(z), \psi_z^{i,k}(z))$, and $l^{M,k}$ corresponds to the jump of the flux of the solutions at $z = z_i$. Specifically:

$$\begin{aligned} l^{M,1}(\mathbf{F}) &= 2\left(F_-(z_i)\right)^*, \\ l^{M,2}(\mathbf{F}) &= 2\left(F_+(z_i)\right)^*, \\ &\text{for } i = 1, \cdots, (N-1). \end{aligned} \tag{60}$$

Similarly to the local primary field, we consider the extension by zero of the local solutions on Ω_z, and we have $\boldsymbol{\psi}^{i,k} \in V_0(\Omega_z)$. We denote the solutions of these local problems as multi-scale basis functions. We define the following space of multi-scale basis functions:

$$V_M = \text{span}\left\{ \left\{ \boldsymbol{\psi}^{i,k}(z) = \left(\psi_-^{i,k}(z), \psi_+^{i,k}(z), \psi_z^{i,k}(z)\right) \right\}_{i=1}^{N-1} \right\}_{k=1}^{2}. \tag{61}$$

5. **Solve the secondary field formulation using the multi-scale basis functions**. Since the flux components of the local primary field are discontinuous, we need our secondary field to balance these artificial discontinuities. Thus, by combining the primary and secondary fields, we recover a continuous flux for the full field. From (56), we obtain:

$$b(\mathbf{F}, \mathbf{H}^S) = b(\mathbf{F}, \mathbf{H}) - b(\mathbf{F}, \mathbf{H}^P) = l(\mathbf{F}) - b(\mathbf{F}, \mathbf{H}^P),\ \mathbf{F} \in V_0(\Omega_z). \tag{62}$$

We describe our secondary field as follows:

$$\mathbf{H}^S(z) = \sum_{i=1}^{N-1} \sum_{k=1}^{2} \alpha_{i,k} \boldsymbol{\psi}^{i,k}(z), \tag{63}$$

where $\mathbf{H}^S = (H_-^S, H_+^S, H_z^S)$, and $\boldsymbol{\psi}^{i,k} \in V_M$. By the definition of the multi-scale basis functions, (63) satisfies the reduced wave equation. Moreover, we consider $\mathbf{F} \in V_M$. Therefore, by substituting (63) into (62), we have:

$$\begin{aligned} \sum_{i=1}^{N-1} \sum_{k=1}^{2} \alpha_{i,k} b(\boldsymbol{\psi}^{m,n}, \boldsymbol{\psi}^{i,k}) &= l(\boldsymbol{\psi}^{m,n}) - b(\boldsymbol{\psi}^{m,n}, \mathbf{H}^P), \\ &m = 1, \cdots, (N-1),\ n = 1, 2. \end{aligned} \tag{64}$$

Finally, we add the local primary field and the secondary field to evaluate the full field.

In the next sections, we further describe the formulation for each step.

4.1. Local primary field

We consider the local primary field defined in Equation (57). We further decompose our primary field as follows:

$$\mathbf{H}^P = \mathbf{H}^F\Big|_{\Omega_p} + \mathbf{H}^C, \tag{65}$$

where $\mathbf{H}^F$ is the fundamental solution of the electromagnetic reduced wave equation, and $\mathbf{H}^C$ is a correction field.

Since the fundamental field has no boundary condition at the boundaries of Ω_p, the correction field is intended to enforce the zero Dirichlet (tangential) boundary condition on $\mathbf{H}^P$ (see Figure 4). We define our correction field as follows:

$$\mathbf{H}^C = \sum_{i=p-1}^{p} \sum_{k=1}^{2} \beta_{i,k} \mathbf{H}^{C,i,k}, \tag{66}$$

where $\mathbf{H}^{C,i,k}$ $(i = p-1, p$ and $k = 1, 2)$ are the correction basis functions. To

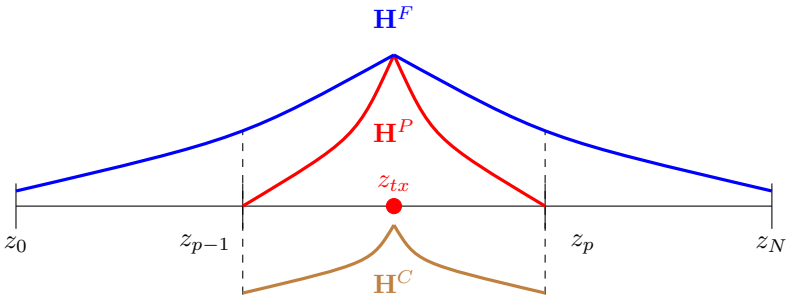

Figure 4: Fundamental, correction and local primary fields.

define them, we perform the following decomposition:

$$\mathbf{H}^{C,i,k} = \mathbf{H}_0^{C,i,k} + \mathbf{H}_1^{C,i,k}, \ i = p-1, p, \ k = 1, 2, \tag{67}$$

where $\mathbf{H}_0^{C,i,k} \in V_0(\Omega_p)$, and $\mathbf{H}_1^{C,i,k} \in V^j(\Omega_p)$, for $j \neq i$, is a lift of the correction field at z_i to impose the non-zero Dirichlet boundary condition. $V^i(\Omega_p) \subset V(\Omega_p)$, for $i = p-1, p$, is the space of all vector-valued functions $\mathbf{F} \in V(\Omega_p)$ satisfying a zero Dirichlet (tangential) boundary condition at $z = z_i$. By substituting (67) into variational formulation (41), we arrive at:

$$b(\mathbf{F}, \mathbf{H}_0^{C,i,k}) = -b(\mathbf{F}, \mathbf{H}_1^{C,i,k}),\ \mathbf{H}_0^{C,i,k},\ \mathbf{F} \in V_0(\Omega_p),\ i = p-1, p,\ k = 1, 2. \quad (68)$$

In order to impose a zero Dirichlet (tangential) boundary condition for our local primary field, we enforce the following conditions:

$$\mathbf{n}_j \times \mathbf{H}^C(z_j) = -\mathbf{n}_j \times \mathbf{H}^F(z_j),\ j = p-1,\ p, \quad (69)$$

where $\mathbf{n}_{p-1} = -\hat{\mathbf{z}}$ and $\mathbf{n}_p = \hat{\mathbf{z}}$ are the outward unit normal vectors at z_{p-1} and z_p, respectively. Using (66), we obtain:

$$\sum_{i=p-1}^{p} \sum_{k=1}^{2} \beta_{i,k} \mathbf{n}_j \times \mathbf{H}^{C,i,k}(z_j) = -\mathbf{n}_j \times \mathbf{H}^F(z_j),\ j = p-1,\ p. \quad (70)$$

4.2. Secondary field formulation

We define the secondary field to be the difference between the full field and the local primary field. Therefore, we have:

$$\mathbf{H}^S = \mathbf{H} - \mathbf{H}^P. \quad (71)$$

Since the flux of the local primary field may be discontinuous on the boundaries of its domain, the flux of the secondary field should be discontinuous on the boundaries of the primary field's domain as follows:

$$[\mathbf{n}_i \times \nabla \times \mathbf{H}^S]_{z_i} = -[\mathbf{n}_i \times \nabla \times \mathbf{H}^P]_{z_i},\ i = p-1,\ p, \quad (72)$$

where $\mathbf{n}_{p-1} = -\hat{\mathbf{z}}$ and $\mathbf{n}_p = \hat{\mathbf{z}}$. Thus, the full field has a continuous flux on Ω_z, since the secondary field satisfies (72). Hence, the secondary field formulation is:

$$\begin{aligned} b(\mathbf{F}, \mathbf{H}^S) = &- (Q \cdot \mathbf{F}(z_{p-1}))^* Q \cdot [\mathbf{n}_{p-1} \times \tilde{\boldsymbol{\sigma}}^{-1}(z) \nabla \times \mathbf{H}^P]_{z_{p-1}} \\ &- (Q \cdot \mathbf{F}(z_p))^* Q \cdot [\mathbf{n}_p \times \tilde{\boldsymbol{\sigma}}^{-1}(z) \nabla \times \mathbf{H}^P]_{z_p}. \end{aligned} \quad (73)$$

We have:

$$\hat{\mathbf{z}} \times \nabla \times \mathbf{H}^P = -\left(\nabla \times \mathbf{H}^P\right)_\phi \hat{\boldsymbol{\rho}} + \left(\nabla \times \mathbf{H}^P\right)_\rho \hat{\boldsymbol{\phi}}. \tag{74}$$

Using the fact that $\mathbf{H}^P(z_{p-1}^-) = \mathbf{0}$, and considering (74), we obtain:

$$\begin{aligned} -\big(Q \times \left[\hat{\mathbf{z}} \times \tilde{\boldsymbol{\sigma}}^{-1}(z)\nabla \times \mathbf{H}^P\right]_{z_{p-1}}\Big)_\rho = \frac{-1}{\sqrt{2\pi}}\tilde{\sigma}_h^{-1}(z_{p-1}^+) \\ \cdot \sum_{m=-\infty}^{+\infty} e^{-im\phi} \int_0^{+\infty} \mathit{\Pi}_- \left(\mathbf{H}^P\right)(z_{p-1}^+) J_{m-1}(\xi\rho)\xi d\xi. \end{aligned} \tag{75}$$

Using the first component of the curl (24), we have:

$$\begin{aligned} -\Big(Q\left[\hat{\mathbf{z}} \times \tilde{\boldsymbol{\sigma}}^{-1}(z)\nabla \times \mathbf{H}^P\right]_{z_{p-1}}\Big)_\phi = \frac{-i}{\sqrt{2\pi}}\tilde{\sigma}_h^{-1}(z_{p-1}^+) \\ \cdot \sum_{m=-\infty}^{+\infty} e^{-im\phi} \int_0^{+\infty} \mathit{\Pi}_+ \left(\mathbf{H}^P\right)(z_{p-1}^+) J_{m+1}(\xi\rho)\xi d\xi. \end{aligned} \tag{76}$$

Similarly, since $\mathbf{H}^P(z_p^+) = \mathbf{0}$, the jump on the right boundary of primary field's domain is equal to:

$$\begin{aligned} \Big(Q\left[\hat{\mathbf{z}} \times \tilde{\boldsymbol{\sigma}}^{-1}(z)\nabla \times \mathbf{H}^P\right]_{z_p}\Big)_\rho = \frac{1}{\sqrt{2\pi}}\tilde{\sigma}_h^{-1}(z_p^-) \\ \cdot \sum_{m=-\infty}^{+\infty} e^{-im\phi} \int_0^{+\infty} \mathit{\Pi}_- \left(\mathbf{H}^P\right)(z_p^-) J_{m-1}(\xi\rho)\xi d\xi, \end{aligned} \tag{77}$$

$$\begin{aligned} \Big(Q\left[\hat{\mathbf{z}} \times \tilde{\boldsymbol{\sigma}}^{-1}(z)\nabla \times \mathbf{H}^P\right]_{z_p}\Big)_\phi = \frac{i}{\sqrt{2\pi}}\tilde{\sigma}_h^{-1}(z_p^-) \\ \cdot \sum_{m=-\infty}^{+\infty} e^{-im\phi} \int_0^{+\infty} \mathit{\Pi}_+ \left(\mathbf{H}^P\right)(z_p^-) J_{m+1}(\xi\rho)\xi d\xi. \end{aligned} \tag{78}$$

By using the orthogonality of the Bessel functions and the exponentials, similar to the computations for (41), we obtain:

$$b(\mathbf{F}, \mathbf{H}^S) = l_p^{S,-}(\mathbf{F}, \mathbf{H}^P) + l_p^{S,+}(\mathbf{F}, \mathbf{H}^P), \text{ for all } \mathbf{F} \in V_0(\Omega_z), \tag{79}$$

where

$$\begin{aligned} l_p^{S,+}(\mathbf{F}, \mathbf{H}^P) =& 2\tilde{\sigma}_h^{-1}(z_p^-)\Big(F_-^* \mathit{\Pi}_- \left(\mathbf{H}^P\right) + F_+^* \mathit{\Pi}_+ \left(\mathbf{H}^P\right)\Big)(z_p^-), \\ l_p^{S,-}(\mathbf{F}, \mathbf{H}^P) =& -2\tilde{\sigma}_h^{-1}(z_{p-1}^+)\Big(F_-^* \mathit{\Pi}_- \left(\mathbf{H}^P\right) + F_+^* \mathit{\Pi}_+ \left(\mathbf{H}^P\right)\Big)(z_{p-1}^+). \end{aligned} \tag{80}$$

Similarly, by considering the jump condition of the flux of multi-scale basis functions, they are computed using (60).

4.3. Global problem

Using (63), (79), and the definition of the multi-scale basis functions, we obtain:

$$b(\mathbf{F}, \mathbf{H}^S) = \sum_{i=1}^{N-1} \sum_{k=1}^{2} \alpha_{i,k} \mathbf{m}(\mathbf{F}, \boldsymbol{\psi}^{i,k}), \tag{81}$$

where, for an arbitrary test function $\mathbf{F}$ and a multi-scale basis function $\boldsymbol{\psi}^{i,k}$:

$$\mathbf{m}(\mathbf{F}, \boldsymbol{\psi}^{i,k}) = 2 \sum_{l=i-1}^{i+1} (Q \cdot \mathbf{F})^* \left[Q \cdot \mathbf{n}_l \times \tilde{\boldsymbol{\sigma}}^{-1}(z) \nabla \times \boldsymbol{\psi}^{i,k} \right]_{z_l}. \tag{82}$$

We consider test functions $\mathbf{F} \in V_M$. Hence, by using (80), we have:

$$\begin{aligned} \sum_{i=1}^{N-1} \sum_{k=1}^{2} \alpha_{i,k} \mathbf{m}(\boldsymbol{\psi}^{m,n}, \boldsymbol{\psi}^{i,k}) = l_p^{S,-}(\boldsymbol{\psi}^{m,n}, \mathbf{H}^P) + l_p^{S,+}(\boldsymbol{\psi}^{m,n}, \mathbf{H}^P), \\ m = 1, \cdots, (N-1), \ n = 1, 2. \end{aligned} \tag{83}$$

By using (23), we can further simplify $\mathbf{m}(.,.)$ to:

$$\mathbf{m}(\boldsymbol{\psi}^{m,n}, \boldsymbol{\psi}^{i,k}) = \sum_{l=1}^{N-1} \sum_{s=-,+} (\psi_s^{m,n}(z_l))^* \left[\tilde{\sigma}_h^{-1}(z) \Pi_s(\boldsymbol{\psi}^{i,k}) \right]_{z_l}. \tag{84}$$

5. Implementation

For simplicity and to compare our numerical method directly with the state-of-the-art analytic implementations, we assume $\boldsymbol{\mu} = \mu_0 \mathbf{I}_3$ and $\boldsymbol{\varepsilon} = \varepsilon_0 \mathbf{I}_3$ ($\mathbf{I}_3$ is the 3D identity matrix) to be constant in each layer. ε_0 is set to $8.85 \times 10^{-12}(F/m)$, which corresponds to the free-space permittivity, while μ_0 is set to $4\pi \times 10^{-7}(H/m)$, i.e., the magnetic permeability constant.

We consider each layer as a sub-domain. Therefore, the decomposition points are the boundaries of our layers. By doing so, we can evaluate the local primary fields in sub-domains which have smoothly varying materials. In particular, if we assume that the materials are homogeneous and constant, the fundamental solution in (65) is independent of the tool position. Moreover, the correction basis functions are independent of the tool position. Consequently, instead of solving one primary field for each tool position, we find one fundamental field

and four correction basis functions per layer. This simplification allows us to increase the speed of the method almost by a factor equal to the number of tool positions.

In our model problem, we consider two different Cartesian coordinate systems: (a) a system of coordinates related to the Earth, and (b) a system of coordinates related to the borehole, which consists of a rotation of the Earth system of coordinates in a way that the borehole extends along the z direction. We denote the angle between the borehole and the z direction of the Earth system of coordinates as α (dip angle). β is the azimuthal angle (see Figure 5). Therefore, the transformation between the systems of coordinates of the Earth and the borehole is given by the following rotation matrix:

$$\boldsymbol{\mathcal{H}}_b = \mathbf{R}^{-1}\boldsymbol{\mathcal{H}}_e\mathbf{R}, \tag{85}$$

where rotation $\mathbf{R}$ is defined by the following composition of rotations:

$$\mathbf{R} = \begin{bmatrix} \cos\beta & -\sin\beta & 0 \\ \sin\beta & \cos\beta & 0 \\ 0 & 0 & 1 \end{bmatrix} \cdot \begin{bmatrix} \cos\alpha & 0 & \sin\alpha \\ 0 & 1 & 0 \\ -\sin\alpha & 0 & \cos\alpha \end{bmatrix}.$$

In this notation, subscripts e and b denote the Earth system of coordinates and the borehole system of coordinates, respectively. If the borehole is perpendicular to the layering of the medium, we have $\alpha = 0$.

In this work, for simplicity, we consider $\beta = 0$. Hence, the possibly non-zero components of the magnetic field can only be $\mathcal{H}_{xx}$, $\mathcal{H}_{xz}$, $\mathcal{H}_{yy}$, $\mathcal{H}_{zx}$ and $\mathcal{H}_{zz}$, where the first and the second letters in the subscript indicate the transmitter and receiver directions, respectively.

In order to analyze the result of our experiments and compare them against those typically obtained in borehole resistivity applications, we further post-process the values of the magnetic field. First, we evaluate the zz-component ($\mathcal{H}_{zz}$) of the magnetic field at two different receivers. We denote these values as $\mathcal{H}_{zz}(Rx_1)$ and $\mathcal{H}_{zz}(Rx_2)$, which correspond to the first and the second receiver,

respectively. Then, we compute:

$$\log \frac{\mathcal{H}_{zz}(Rx_1)}{\mathcal{H}_{zz}(Rx_2)} = \underbrace{\log \frac{\mid \mathcal{H}_{zz}(Rx_1) \mid}{\mid \mathcal{H}_{zz}(Rx_2) \mid}}_{\text{attenuation}} + i \underbrace{(ph(\mathcal{H}_{zz}(Rx_1)) - ph(\mathcal{H}_{zz}(Rx_2)))}_{\text{phase difference}}, \quad (86)$$

where ph denotes the phase of a complex number. Subsequently, we compute the relation between attenuation and resistivity in a homogeneous media. This transformation, when applied to a heterogeneous media, delivers the *apparent resistivity* based on attenuation (see [1]). We similarly define the apparent resistivity based on the phase difference.

For the inverse Hankel transform, we use a fast Hankel transform algorithm based on digital filters (see [21] for details).

The entire Hankel Finite Element method has been implemented using *FORTRAN 90*.

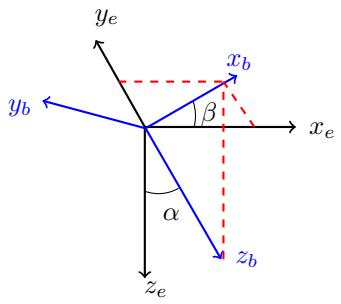

Figure 5: x_e, y_e and z_e are the axes of the Cartesian coordinates. x_b, y_b and z_b are the axes of the borehole coordinates. α and β are the dip and azimuthal angles, respectively.

6. Numerical examples

6.1. Model problem 1: Two layers with 1 $\Omega \cdot m$ and 100 $\Omega \cdot m$

We consider the logging instrument described in Figure 6. Figures 7 through 9 show the apparent resistivities (logs) for different dip angles. The distance between two consecutive logging points is half a foot (0.1524 m). In all cases, our simulation framework delivers a perfect agreement with the semi-analytic solutions.

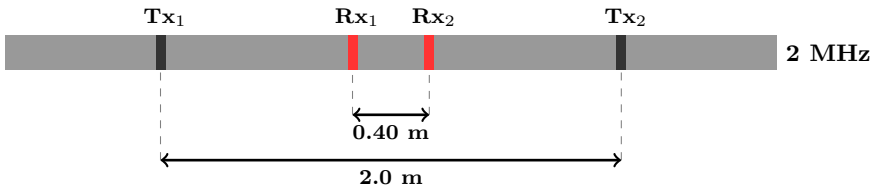

Figure 6: Logging instrument for model problem 1. Tx_1 and Tx_2 are the transmitters, and Rx_1 and Rx_2 are the receivers.

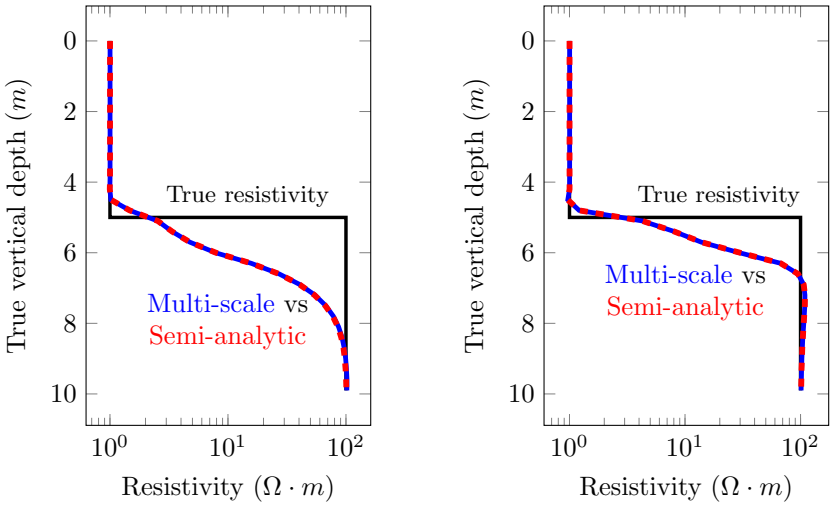

(a) Apparent resistivity based on attenuation

(b) Apparent resistivity based on phase difference

Figure 7: Model problem 1. Apparent resistivities for the zz-component for a vertical well (dip angle = 0°).

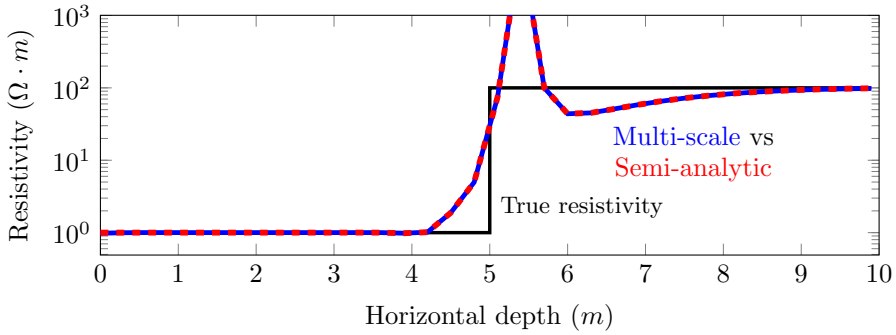

(a) Apparent resistivity based on attenuation

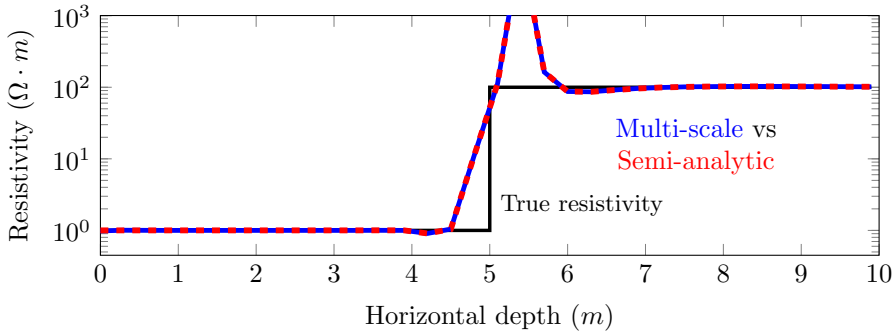

(b) Apparent resistivity based on phase difference

Figure 8: Model problem 1. Apparent resistivity for the zz-component for a 70° deviated well.

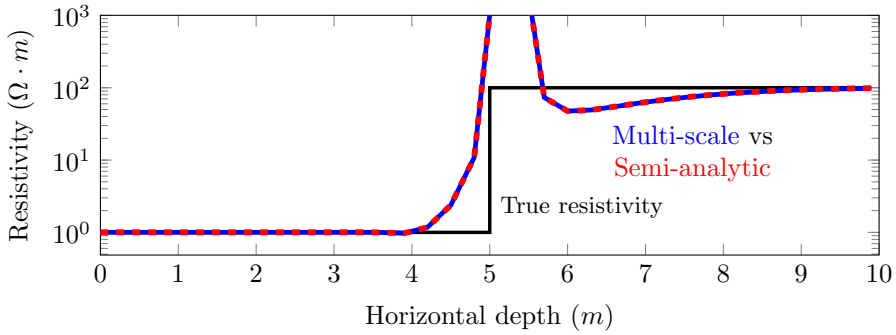

(a) Apparent resistivity based on attenuation

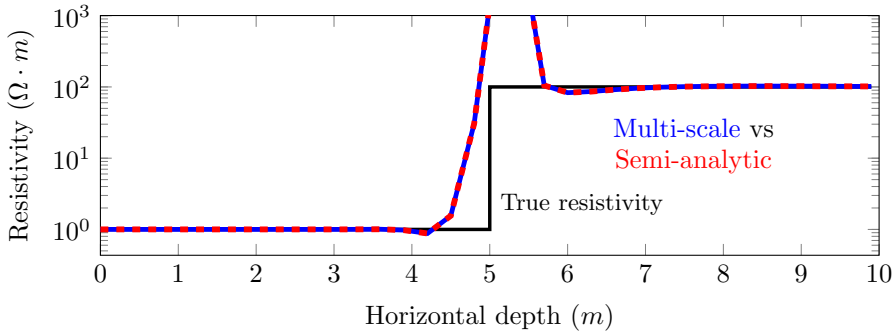

(b) Apparent resistivity based on phase difference

Figure 9: Model problem 1. Apparent resistivity for the zz-component for a 89° deviated well.

6.2. Model problem 2: Multilayered formation.

Figure 10 describes the logging instrument employed for this example. As in our previous examples, the distance between two consecutive logging points is half a foot (0.1524 m). The main result in terms of apparent resistivities for this model problem for a vertical well is shown in Figure 11. The attenuations and phase differences for this case are shown in Figures 12 and 13, respectively. As before, the numerical solutions coincide with the semi-analytic ones.

Table 1 shows a time comparison between a semi-analytic method and the proposed numerical method. For one tool position, computing the local primary field and pre-computing the multi-scale basis functions is computationally ex-

pensive and we observe a large discrepancy between numerical and semi-analytic solutions. However, as expected, by increasing the number of tool positions, the ratio between the time of the proposed numerical method and the semi-analytic one is decreasing. Figure 14 shows the average time used to solve one tool position. Using a multi-scale method, the average time per position rapidly decreases as we augment the total number of tool positions. This occurs because the pre-computed multi-scale basis functions, fundamental fields, and correction basis functions only need to be computed once for any number of tool positions.

The results in terms of apparent resistivities for this model problem for 60° and 89° deviated wells are shown in Figures 15 and 16, respectively. Again, the numerical and semi-analytic solutions coincide.

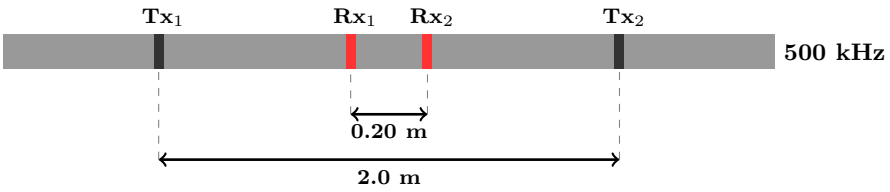

Figure 10: Logging instrument for model problem 2. Tx_1 and Tx_2 are the transmitters, and Rx_1 and Rx_2 are the receivers.

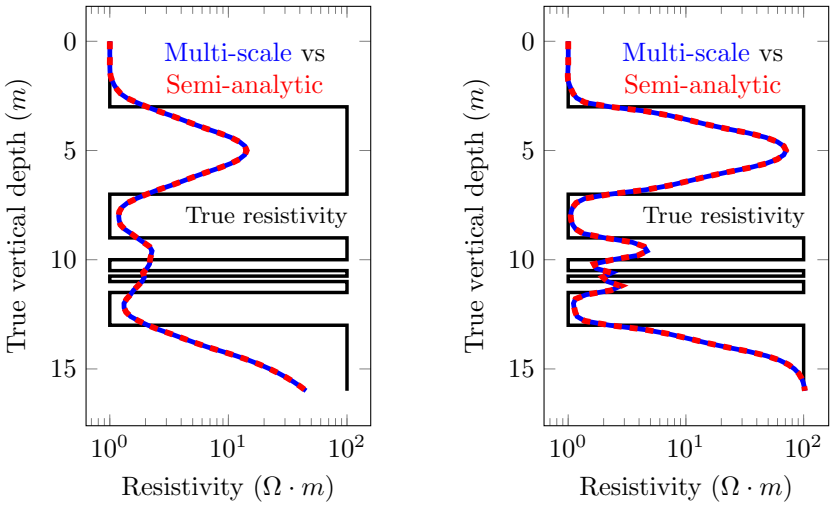

(a) Apparent resistivity based on attenuation

(b) Apparent resistivity based on phase difference

Figure 11: Model problem 2. Apparent resistivity for the zz-component for a vertical well (dip angle = 0°).

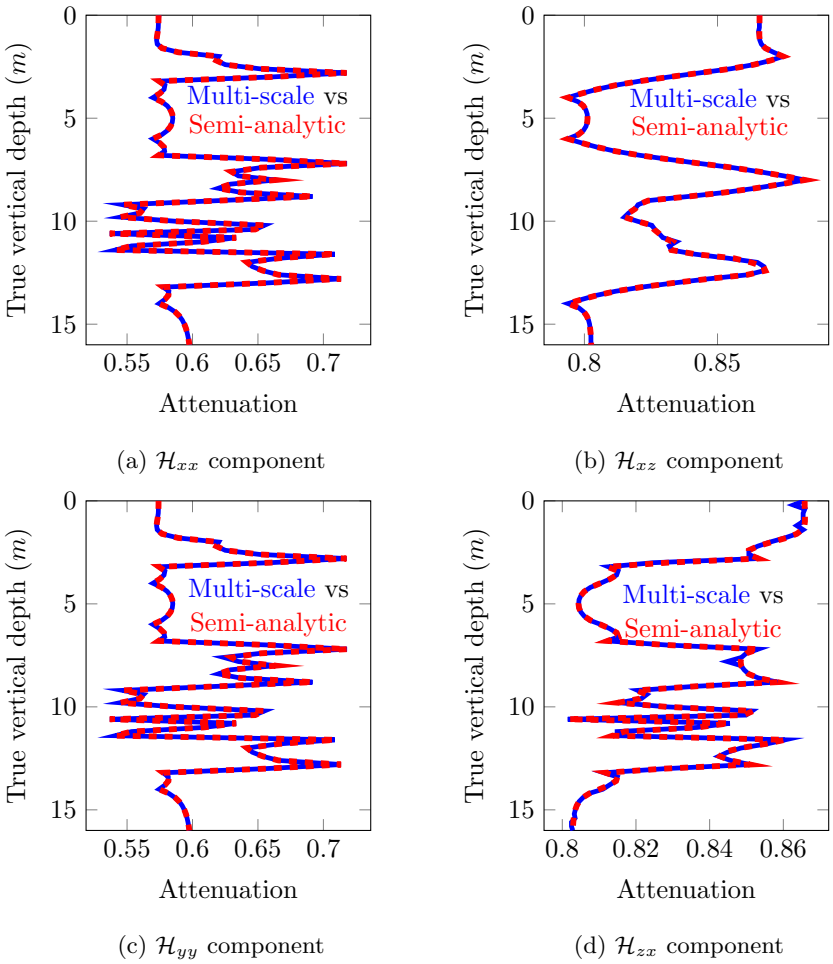

(a) $\mathcal{H}_{xx}$ component

(b) $\mathcal{H}_{xz}$ component

(c) $\mathcal{H}_{yy}$ component

(d) $\mathcal{H}_{zx}$ component

Figure 12: Model problem 2. Attenuations for the non-zero components ($\mathcal{H}_{xx}$, $\mathcal{H}_{xz}$, $\mathcal{H}_{yy}$ and $\mathcal{H}_{zx}$) of the magnetic field for a vertical well (dip angle = 0°).

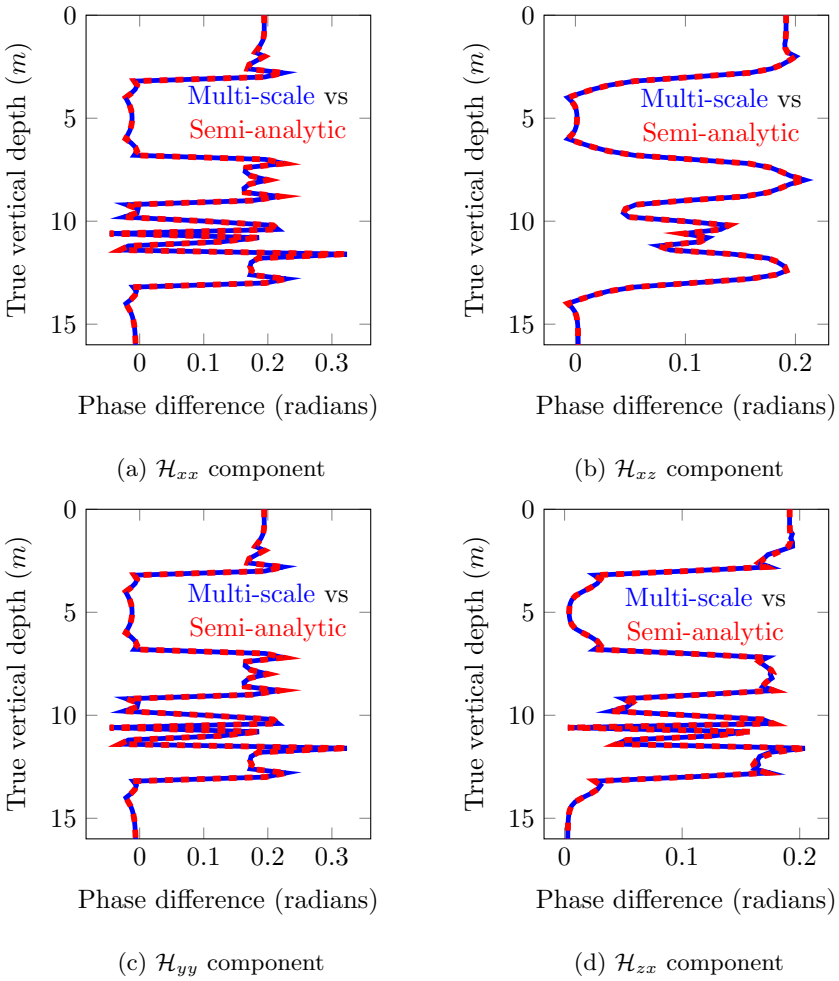

(a) $\mathcal{H}_{xx}$ component

(b) $\mathcal{H}_{xz}$ component

(c) $\mathcal{H}_{yy}$ component

(d) $\mathcal{H}_{zx}$ component

Figure 13: Model problem 2. Phase differences for the non-zero components ($\mathcal{H}_{xx}$, $\mathcal{H}_{xz}$, $\mathcal{H}_{yy}$ and $\mathcal{H}_{zx}$) of the magnetic field for a vertical well (dip angle = 0°).

Positions	Semi-analytic	Numerical	Ratio
1	3.2×10^{-2}	6.54	204.37
10	5.3×10^{-2}	13.53	256.60
100	1.4×10^{-1}	19.5	139.28
200	2.4×10^{-1}	24.92	103.04
500	4.1×10^{-1}	39.34	95.95
1000	1.01	53.02	52.49
5000	5.68	117.32	20.65
10000	11.57	207.61	17.94

Table 1: A time comparison (in seconds) for a vertical well using a semi-analytic method and the proposed multi-scale FEM as a function of the number of tool positions.

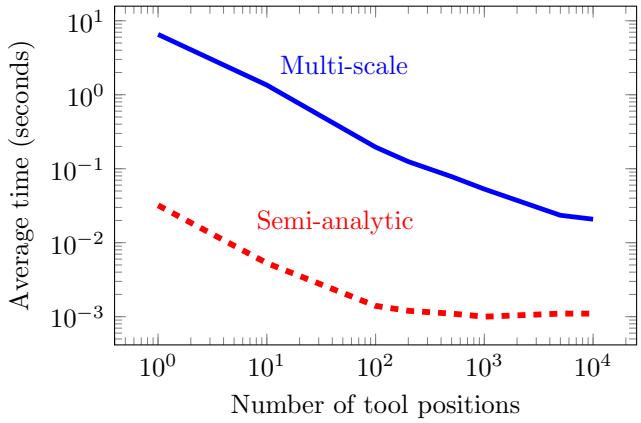

Figure 14: Model problem 2. Average time (in seconds) to solve for one tool position as the number of tool positions varies ($\frac{\text{time(seconds)}}{\text{number of tool positions}}$).

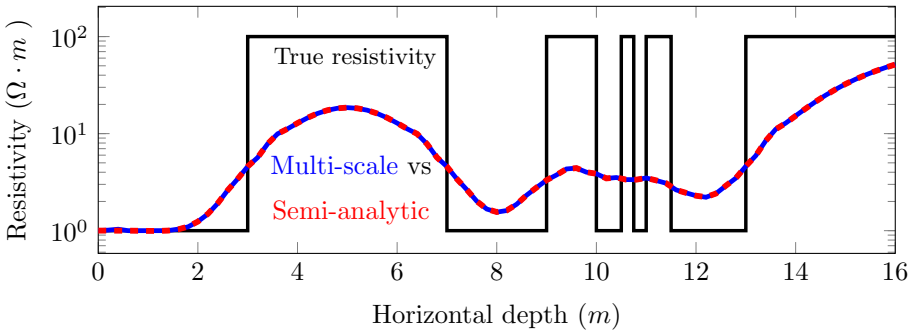

(a) Apparent resistivity based on attenuation

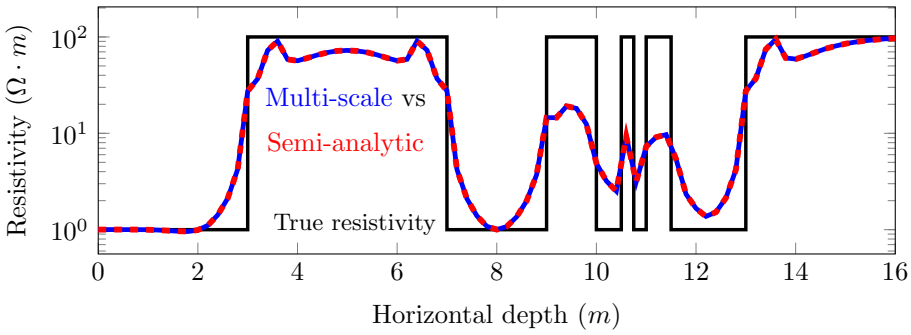

(b) Apparent resistivity based on phase difference

Figure 15: Model problem 2. Apparent resistivity for the zz-component for a 60° deviated well.

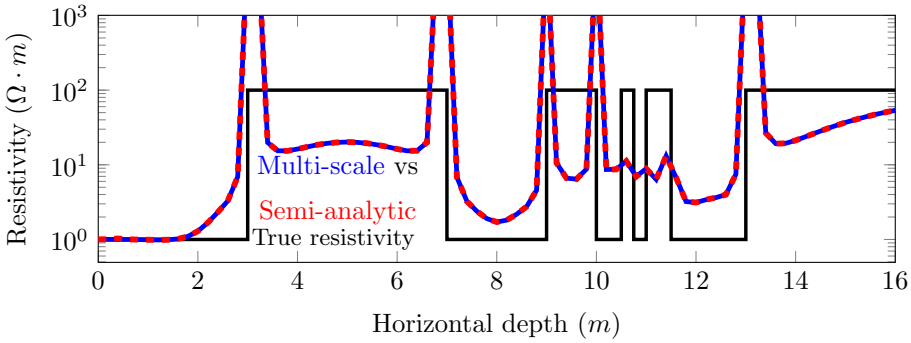

(a) Apparent resistivity based on attenuation

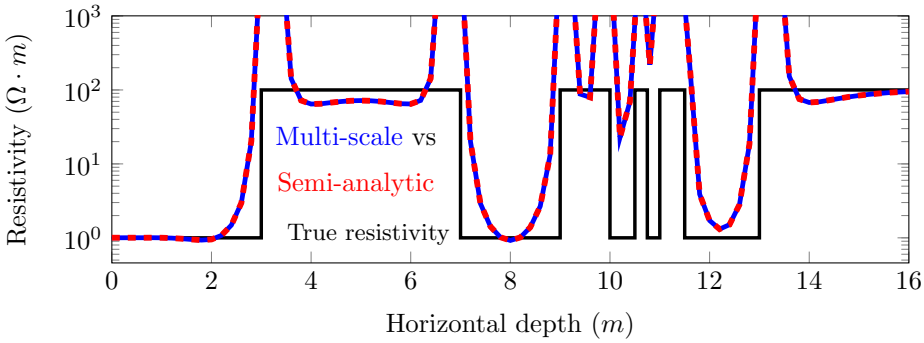

(b) Apparent resistivity based on phase difference

Figure 16: Model problem 2. Apparent resistivity for the zz-component for a 89° deviated well.

6.3. Model problem 3: Non-piecewise-constant resistivity distribution

We consider the logging instrument described in Figure 6 and a model problem that exhibits a sub-domain with a linearly varying resistivity. The numerical solution for this example for a vertical well is illustrated in Figure 17. For this case, the semi-analytic solution is unknown.

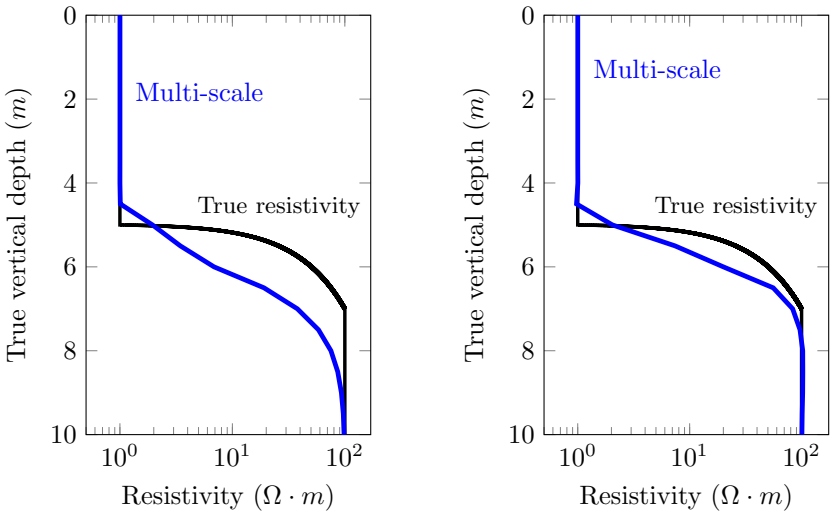

(a) Apparent resistivity based on attenuation

(b) Apparent resistivity based on phase difference

Figure 17: Model problem 3. Apparent resistivity for the zz-component for a vertical well (dip angle = 0°).

7. Conclusions

We propose a multi-scale Hankel FEM for solving Maxwell's equations in a 1D Transversely Isotropic media excited by a 3D arbitrarily oriented point dipole. The multi-scale FEM pre-computes the fundamental fields, and correction and multi-scale basis functions. As a result, this computation is expensive if only a single logging position is studied, but it becomes competitive as the number of logging position grows.

The numerical method produces highly accurate solutions, as our numerical validations experiments show. Additionally, computation of the parametrization derivatives is straightforward by simply considering the adjoint formulation. This numerical method is able to consider arbitrary resistivity distributions along the z direction, while semi-analytic methods only allow for piecewise constant material coefficients.

As future work, we plan to extend our method to other multi-physics problems e.g. elasto-acoustic problems and to account for other material parameter distributions, such as, cross-bedded formations.

8. Acknowledgement

This work has received funding from the European Union's Horizon 2020 research and innovation programme under the Marie Sklodowska-Curie grant agreement No 644602, the Projects of the Spanish Ministry of Economy and Competitiveness with reference MTM2016-76329-R (AEI/FEDER, EU), and MTM2016-81697-ERC/AEI, the BCAM "Severo Ochoa" accreditation of excellence SEV-2013-0323, and the Basque Government through the BERC 2014-2017 program, the Consolidated Research Group Grant IT649-13 on "Mathematical Modeling, Simulation, and Industrial Applications (M2SI)". This publication was also made possible in part by the CSIRO Professorial Chair in Computational Geoscience at Curtin University and the Deep Earth Imaging Enterprise Future Science Platforms of the Commonwealth Scientific Industrial Research Organisation, CSIRO, of Australia. Additional support was provided by the European Union's Horizon 2020 Research and Innovation Program of the Marie Sklodowska-Curie grant agreement No. 644202, the Mega-grant of the Russian Federation Government (N 14.Y26.31.0013), and The Institute for Geoscience Research (TIGeR) and the Curtin Institute for Computation at Curtin University.

Appendices

A. Bessel functions

Bessel functions are solutions of the following ordinary differential equation:

$$x^2y'' + xy' + (x^2 - m^2)y = 0,$$

where m is a parameter. Bessel functions exhibit multiple interesting properties (see, e.g., [19]). In this work, we employ the following ones:

$$\frac{2m}{\xi\rho}J_m(\xi\rho) = J_{m-1}(\xi\rho) + J_{m+1}(\xi\rho), \tag{87}$$

$$2\frac{\partial J_m(\xi\rho)}{\partial\,(\xi\rho)} = J_{m-1}(\xi\rho) - J_{m+1}(\xi\rho), \tag{88}$$

$$\int_0^{+\infty} J_m(\xi\rho)J_m(\xi_q\rho)\rho\,d\rho = \frac{1}{\xi_q}\delta(\xi,\xi_q). \tag{89}$$

Using (88) for the derivative of J_{m+1} and multiplying the result by ξ, we obtain:

$$\xi\frac{\partial J_{m+1}(\xi\rho)}{\partial\,(\xi\rho)} = \frac{\xi}{2}J_m(\xi\rho) - \frac{\xi}{2}J_{m+2}(\xi\rho). \tag{90}$$

By using (87) for J_{m+2}, we have:

$$J_{m+2}(\xi\rho) = \frac{2(m+1)}{\xi\rho}J_{m+1}(\xi\rho) - J_m(\xi\rho). \tag{91}$$

By substituting (91) into (90), we obtain:

$$\frac{m+1}{\rho}J_{m+1}(\xi\rho) + \xi\frac{\partial J_{m+1}(\xi\rho)}{\partial\,(\xi\rho)} = \xi J_m(\xi\rho). \tag{92}$$

Utilizing (88) for the derivative of J_{m+1}, we arrive at:

$$2\frac{\partial J_{m+1}(\xi\rho)}{\partial\,(\xi\rho)} = J_m(\xi\rho) - J_{m+2}(\xi\rho). \tag{93}$$

By substituting (93) into (92), we conclude:

$$\frac{m+1}{\rho}J_{m+1}(\xi\rho) = \frac{\xi}{2}J_m(\xi\rho) + \frac{\xi}{2}J_{m+2}(\xi\rho). \tag{94}$$

References

[1] D. Pardo, C. Torres-Verdin, Fast 1D inversion of logging-while-drilling resistivity measurements for the improved estimation of formation resistivity in high-angle and horizontal wells, Geophysics 80 (2) (2014) E111–E124.

[2] E. Kausel, Fundamental solutions in elastodynamics: a compendium, Cambridge University Press, 2006.

[3] J. A. Kong, Electromagnetic wave theory, Wiley-Interscience, 1986.

[4] S. H. Ward, G. W. Hohmann, Electromagnetic methods in applied geophysics: volume 1, theory, Society of Exploration Geophysicists, 1987.

[5] A. Kirscha, F. Hettlich, The mathematical theory of time-harmonic Maxwell's equations, Vol. 190, Springer, Switzerland, 2015.

[6] G. L. Wang, T. Barber, P. Wu, D. Allen, A. Abubakar, Triaxial induction tool response in dipping and crossbedded formations, Society of Exploration Geophysicists (2014) 585–590.

[7] S. Davydycheva, D. Homan, G. Minerbo, Triaxial induction tool with electrode sleeve: FD modeling in 3D geometries, Journal of Applied Geophysics 67 (2004) 98–108.

[8] O. Ijasan, C. Torres-Verdín, W. E. Preeg, Inversion-based petrophysical interpretation of logging-while-drilling nuclear and resistivity measurements, Geophysics 78 (6) (2013) D473–D489.

[9] R. Streich, M. Becken, Sensitivity of controlled-source electromagnetic fields in planarly layered media, Geophysical Journal International 187 (2011) 705–728.

[10] S. Constable, L. J. Srnka, An introduction to marine controlled-source electromagnetic methods for hydrocarbon exploration, Geophysics 72 (2) (2007) WA3–WA12.

[11] K. Key, 1D inversion of multicomponent, multifrequency marine CSEM data: methodology and synthetic studies for resolving thin resistive layers, Geophysics 74 (2) (2009) F9–F20.

[12] L. O. Loseth, B. Ursin, Electromagnetic fields in planarly layered anisotropic media, Geophysical Journal International 170 (2007) 44–F80.

[13] S. A. Bakr, D. Pardo, T. Mannseth, Domain decomposition Fourier FE method for the simulation of 3D marine CSEM measurements, Journal of Computational Physics 255 (2013) 456–470.

[14] A. D. Chave, Numerical integration of related Hankel transforms by quadrature and continued fraction expansion, Geophysics 48 (12) (1983) 1671–1686.

[15] S. A. Bakr, D. Pardo, A multi-domain decomposition-based Fourier finite element method for the simulation of 3D marine CSEM measurements, Computational Geosciences 21 (3) (2017) 345–357.

[16] S. A. Bakr, A 2.5D finite element method for modeling of electromagnetic tensor Green's functions on a triangular mesh, Uni Research, Centre for Integrated Petroleum Research 1 (2012) 1–32.

[17] D. Pardo, M. J. Nam, C. Torres-Verdin, M. G. Hoversten, I. Garay, Simulation of marine controlled source electromagnetic measurements using a parallel Fourier *hp*-finite element method, Computational Geosciences 15 (2011) 53–67.

[18] A. D. Chave, C. S. Cox, Controlled electromagnetic sources for measuring electrical conductivity beneath the oceans: part 1. Forward problem and model study, Journal of Geophysical Research 87 (B7) (1982) 5327–5338.

[19] M. Abramowitz, I. A. Stegun, Handbook of mathematical functions with formulas, graphs and mathematical tables, National Bureau of Standard, 1964.

[20] R. Lehe, M. Kirchen, I. A. Andriyash, B. B. Godfrey, J. L. Vay, Quasi-cylindrical and dispersion-free particle-in-cell algorithm, Computer Physics Communications 203 (2013) 66–82.

[21] K. Key, Is the fast Hankel transform faster than quadrature?, Computer Physics Communications 77 (3) (2012) F21–F30.

[22] S. Rojas, I. Muga, D. Pardo, A quadrature-free method for simulation and inversion of 1.5D direct current (DC) borehole measurements, Computational Geosciences 20 (6) (2016) 1301–1318.

[23] I. Muga, S. Ossandón, A method to compute the surface Green's function of piezoelectric half-space, Scientia 13 (2006) 84–91.

[24] S. Davydycheva, T. Wang, A fast modelling method to solve Maxwell's equations in 1D layered biaxial anisotropic medium, Geophysics 76 (5) (2011) F293–F302.

[25] L. Demkowicz, Finite element methods for Maxwell's equations, Encyclopedia of Computational Mechanics (2004) 1 – 26.